Lattice vibrational modes and phonon thermal conductivity of monolayer MoS_2

Yongqing Cai, Jinghua Lan, Gang Zhang,* and Yong-Wei Zhang
*Institute of High Performance Computing, A*STAR, Singapore 138632*
(Received 9 December 2013; revised manuscript received 17 January 2014; published 31 January 2014)

The anharmonic behavior of phonons and intrinsic thermal conductivity associated with the umklapp scattering in monolayer MoS_2 sheet are investigated via first-principles calculations within the framework of density functional perturbation theory. In contrast to the negative Grüneissen parameter (γ) occurring in low-frequency modes in graphene, positive γ in the whole Brillouin zone is demonstrated in monolayer MoS_2 with much larger γ for acoustic modes than that for the optical modes, suggesting that monolayer MoS_2 sheet possesses a positive coefficient of thermal expansion. The calculated phonon lifetimes of the infrared active modes are 5.50 and 5.72 ps for E' and A_2'', respectively, in good agreement with experimental results obtained by fitting the dielectric oscillators with the infrared reflectivity spectrum. The lifetime of the Raman A_1' mode (38.36 ps) is about seven times longer than those of the infrared modes. The dominated phonon mean free path of monolayer MoS_2 is less than 20 nm, about 30-fold smaller than that of graphene. Combined with the nonequilibrium Green's function calculations, the room temperature thermal conductivity of monolayer MoS_2 is found to be around 23.2 $W\,m^{-1}\,K^{-1}$, two orders of magnitude lower than that of graphene.

DOI: 10.1103/PhysRevB.89.035438 PACS number(s): 63.20.dk, 65.80.−g, 63.22.−m

I. INTRODUCTION

As a semiconducting analog of graphene, the atomically thin MoS_2 monolayer, consisting of a hexagonal lattice of Mo atoms sandwiched between two similar lattices of S atoms in a trigonal prismatic arrangement, has recently attracted considerable attention for field effect transistor (FET) and optical device applications due to the presence of a finite band gap [1,2]. Great efforts have been made to understand the dynamics of carriers of MoS_2 including mobilities of excitons [3,4], electrons/holes [5,6], and the effects from electrical [7] and stress [8–10] fields applied within the layers. In contrast to graphene, dielectric screening associated with the electron-electron interaction and electron-phonon coupling of the inter- and intralayers gives rise to an anomalous frequency shift [11], a symmetry-dependent phonon renormalization [12], and a superconducting behavior in MoS_2 [13].

In addition to the potential applications in FET devices, MoS_2 has recently shown an intriguing capability of a thermoelectric energy conversion, where a large value of the Seebeck coefficient for single-layer MoS_2 (-4×10^2 and $-1 \times 10^5\,\mu V\,K^{-1}$ depending on the strength of the external electric field) was demonstrated [14]. For both FET and thermoelectric applications, the phonon property of monolayer or few-layer (FL) MoS_2 is critical. On the one hand, the electron-acoustic phonon coupling dominates the scattering of low-energy carriers, which limits the carrier mobility [5,6]. On the other hand, monolayer MoS_2 is a semiconductor with a sizable band gap. Thus the electrons have limited contribution to thermal conductivity (κ), and the intrinsic κ is dominated by phonon contribution. Recent molecular-dynamics (MD) simulations showed that the κ value for monolayer MoS_2 is 1.35 $W\,m^{-1}\,K^{-1}$ by Liu *et al.* [15] and 6 $W\,m^{-1}\,K^{-1}$ by Jiang *et al.* [16]. Experimental measurements of the κ of FL MoS_2 were reported to be between 0.4 and 1.59 $W\,m^{-1}\,K^{-1}$ [17,18]. More recently, using the Raman spectroscopy approach, Sahoo *et al.* reported a value of around 52 $W\,m^{-1}\,K^{-1}$ for FL MoS_2 [19]. Compared to the extensive studies on the thermal conductivity of graphene [20–23], comprehensive analysis of the Grüneissen parameter, phonon relaxation time, and phonon mean free path (MFP) of MoS_2 is currently still lacking, despite their critical role in the understanding of the phonon scattering, temperature effect, and phonon-mode contribution to the intrinsic thermal conductivity.

In this study, by using density functional perturbation theory (DFPT), we investigate the lifetime of phonons, and intrinsic κ of monolayer MoS_2 by calculating the Grüneissen parameters, frequency- and polarization-dependent phonon relaxation time, and MFP. Positive Grüneissen parameters for all the modes, in contrast to the negative Grüneissen of the low-frequency mode in graphene, are found for monolayer MoS_2. The calculated dominated MFP of MoS_2 is around 18.1 nm. Based on the nonequilibrium Green's function (NEGF) scheme, the intrinsic κ at room temperature is found to be around 23.2 $W\,m^{-1}\,K^{-1}$. Our study shows that, owing to the S-Mo-S sandwich structure, the single-layer MoS_2 is dramatically different from the one-atom-thick graphene with respect to the structural stability, thermal expansion, vibrating anharmonic behavior, and thermal conductivity.

II. COMPUTATIONAL METHOD

The calculations of the interatomic force constants (IFC) and phonon dispersion are performed using the QUANTUM-ESPRESSO code [24], within the local density approximation (LDA) of Perdew and Wang. We use the norm-conserving pseudopotential with energy (charge density) cutoff up to 70 Ry (700 Ry). The first Brillouin zone is sampled with a $30 \times 30 \times 1$ Monkhorst-Pack grid. The vacuum region thickness is greater than 16 Å. The structures are relaxed until the forces exerted on the atoms are <0.01 eV/Å. The optimized equilibrium lattice constant of monolayer MoS_2 is 3.09 Å, smaller than the measured value of 3.16 Å [25] as LDA normally underestimates the lattice constant. In the following DFPT calculation, a Monkhorst-Pack $10 \times 10 \times 1$ $\boldsymbol{q}$ mesh is

*zhangg@ihpc.a-star.edu.sg

used to calculate the dynamical matrix at each $\boldsymbol{q}$ grid, which gives the IFC through inverse Fourier transform to real space.

The thermal conductance is calculated based on the NEGF approach [26,27]. The ballistic thermal conductance of a junction connected to two leads at different equilibrium heat-bath temperatures is given by the Landauer formula

$$\sigma(T) = \int_0^\infty \hbar\omega T[\omega] \frac{\partial f_B(\omega,T)}{\partial T} \frac{d\omega}{2\pi}, \quad (1)$$

where $f_B(\omega,T) = 1/(e^{\hbar\omega/k_BT} - 1)$ is the Bose-Einstein distribution function for a phonon with a frequency at the reservoirs, $T[\omega]$ is the transmission coefficient, $\hbar$ is Planck's constant, and T is the average temperature of the hot and cold baths. Within the framework of NEGF, the phonon-transmission function $T[\omega]$ is given by $T[\omega] = \mathrm{Tr}[G^r\Gamma_L G^a \Gamma_R]$, where G^r and G^a are, respectively, the retarded and advanced Green's functions of the central region connected with two leads defined as $G^r = (G^a)^+ = [\omega^2 - K^c - \Sigma_L^r - \Sigma_R^r]^{-1}$ with K^c being the force constant matrix and L (R) denoting the left (right) leads, $\Gamma_\alpha(\alpha = L \mathrm{and} R)$ is the broadening function describing the ability of phonons to enter and leave the leads and given by $\Gamma_\alpha = i(\Sigma_\alpha^r - \Sigma_\alpha^a)$, where Σ_α^r and Σ_α^a are the self-energies of the leads accounting for coupling of the central part with the leads. Here the IFC is directly calculated by first-principles method.

III. RESULTS AND DISCUSSION

A. Phonon dispersion

The lattice dynamics of bulk and monolayer MoS_2 have been studied both experimentally [11,28–30] and theoretically [31,32]. To facilitate the discussion of the mode-dependent scattering behavior and comparison with experimental results, as inspired by the previous work [33], we summarize the characters of the phonons for both the bulk (2H phase) and monolayer MoS_2 in Fig. 1(a) with respect to the symmetry assignment, frequency, optical character, and eigenvectors. Since the primitive cell of 2H-MoS_2 and monolayer MoS_2 contains six and three atoms, there are a total of 18 and 9 phonon modes, respectively. A factor group analysis of the point group (D_{6h} and D_{3h} for 2H-MoS_2 and monolayer MoS_2, respectively) shows that the long-wavelength optical phonon modes at the Γ point (without the three translational acoustic modes) can be decomposed as

$$\begin{aligned}\Gamma_{\mathrm{optical}}(2\mathrm{H}-\mathrm{MoS_2}) &= A_{2u}(\mathrm{IR}) + E_{1u}(\mathrm{IR}) + A_{1g}(\mathrm{R}) + 2E_{2g}(\mathrm{R}) \\ &\quad + E_{1g}(\mathrm{R}) + 2B_{2g}(\mathrm{IN}) + B_{1u}(\mathrm{IN}) + E_{2u}(\mathrm{IN}); \quad (2a)\end{aligned}$$

$$\begin{aligned}\Gamma_{\mathrm{optical}}(\mathrm{monolayer}) &= A_2''(\mathrm{IR}) + E'(\mathrm{IR}+\mathrm{R}) \\ &\quad + A_2'(\mathrm{R}) + E''(\mathrm{R}), \quad (2b)\end{aligned}$$

where all the Raman (R), infrared (IR), and inactive (IN) modes are assigned. Note that the $A_{2u}, A_{1g}, B_{2g}, B_{1u}, A_2'', A_1'$ modes are singly degenerate and the $E_{1u}, E_{2g}, E_{1g}, E_{2u}, E', E''$ modes are doubly degenerate. The R and IR modes are mutually exclusive in 2H-MoS_2 due to the presence of inversion symmetry in the crystal. The two IR modes in 2H-MoS_2, A_{2u} and E_{1u}, evolve into the IR-active A_2'' and E' modes in the monolayer case, respectively, where the latter is also Raman active due to the lack of inversion center in monolayer and assigned as E_{2g}^1 in bulk or FL MoS_2 [11]. Another out-of-plane A_1g Raman mode in 2H-MoS_2, which is normally used to identify the layer number of FL MoS_2 flakes, matches with the homopolar A_1' mode in the monolayer case, where the top and bottom sulfur layers vibrate out of phase with direction normal to the basal plane while the Mo layer remains stationary. Our calculated frequencies for these modes, listed in Fig. 1(a), are in good agreement with experimental measurements [1,2].

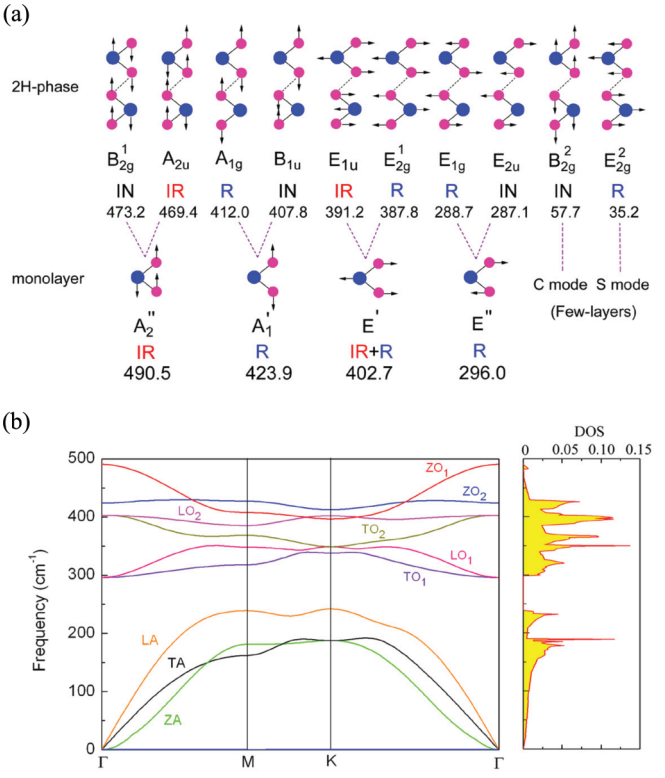

FIG. 1. (Color online) (a) Comparison of the zone-center modes between 2H-MoS_2 and monolayer MoS_2. The frequencies of the 2H phase are adopted from Ref. [32]. (b) Phonon dispersion and phonon DOS for monolayer MoS_2. The polarization of all the phonon branches is presented.

The low-frequency modes B_{2g} and E_{2g} below 60 cm^{-1} (denoted as B_{2g}^2 and E_{2g}^2) in 2H-MoS_2, have no cousin modes in the monolayer. However, the two modes evolve into a series of shear (S) and compression (C) modes in FL MoS_2 spreading around 30 cm^{-1}, respectively [34–37]. These low-energy optical phonons are easily thermally activated at room temperature and believed to greatly affect the carriers mobility and thermal conductivity via electron-phonon scattering and phonon-phonon scattering similar as in FL graphene [38,39]. These interlayer S and C modes in FL MoS_2 show a strong anharmonic character and layer-dependent frequency shift, and have been observed experimentally only recently [37]. We also predict a large Grüneissen parameter of the low-frequency acoustic modes in monolayer as shown below.

The phonon dispersion and density of states (DOS) of the monolayer MoS_2 are shown in Fig. 1(b). There are three acoustic branches: transverse acoustic (TA), longitudinal

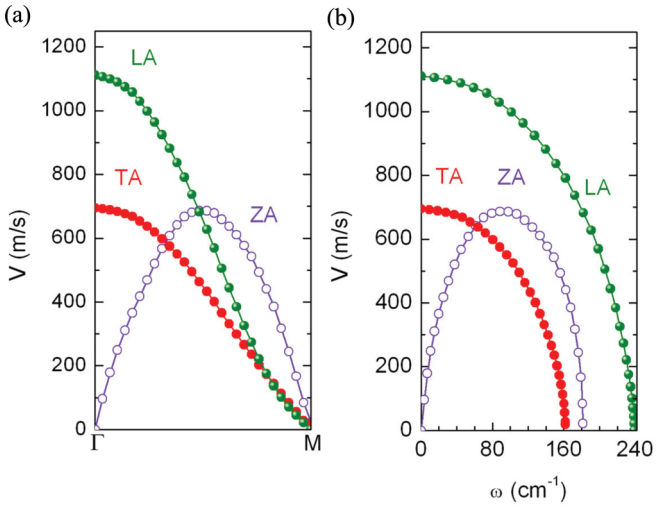

FIG. 2. (Color online) Wave number (a) and frequency (b) -dependent phonon group velocity of acoustic phonon modes along the Γ-M direction.

acoustic (LA), and out-of-plane acoustic (ZA) branches, which are separated by a gap of around 50 cm^{-1} below the nonpolar transverse optical (TO) and longitudinal optical (LO) modes, labeled as TO_1 and LO_1, respectively. The TO_2, LO_2, and ZO_1 modes are three polar branches. The homopolar ZO_2 branch shows a nondispersive behavior, accompanying a breathing mode eigenvector [see A_1' mode in Fig. 1(a)]. In polar semiconductors or insulators, each IR-active mode (polar mode) displays the LO/TO splitting due to the coupling of the lattice to the polarization field created by the polar mode in the long-wavelength limit. For bulk 2H-MoS_2, the Born effective charges of Mo and S are small [33] and the polarized fields associated with the two IR modes (A_{2u} and E_{1u}) are weak (only leading to a 2 cm^{-1} LO/TO splitting [28]) due to a small mode oscillator strength [40,41]. For monolayer MoS_2, the electronic screening is weaker than the three-dimensional case and the splitting will be even smaller and thus is neglected here.

In Fig. 2, we calculate the phonon group velocity $V_n = d\omega_n/dq$ for the nth branch along the Γ-M high symmetrical line. The $V-q$ and $V-\omega$ relationships are plotted in Figs. 2(a) and 2(b), respectively. For the TA and LA modes along the Γ-M direction, the sound velocities at long-wavelength limit are about 693.5 and 1108.8 m/s, respectively, much smaller than the graphene case of 3743 (TA) and 5953 (LA) m/s [23]. For the LA and TA modes, the group velocities drop dramatically with increasing phonon frequency, while for the ZA mode, its group velocity increases with the frequency, reaches maximum at the **q** point sitting at the middle of the Γ-M line, then decreases and finally reaches zero at the zone edge.

B. Grüneissen parameter

The Grüneissen parameter (γ), which provides information on the anharmonic interactions between the lattice waves and the degree of the phonon scattering, is calculated by dilating the lattice with ±0.5% of biaxial strains. For two-dimensional materials, the γ of each phonon mode at $\boldsymbol{q}$ point with s polarization is given by [42,43]

$$\gamma_{\boldsymbol{q}s} = -\frac{a}{2\omega_s(\boldsymbol{q})}\frac{d\omega_s(\boldsymbol{q})}{da}, \tag{3}$$

where a is the relaxed equilibrium lattice constant of 3.09 Å. In Fig. 3, the values of γ for the acoustic and optical modes of MoS_2 are plotted to reflect the mode-dependent strength of anharmonicity.

The values of γ for all the acoustic and optical modes at the Γ point are compiled in Table I. The values of γ for the optical modes are 0.42 (E''), 0.54 (E'), 0.20 (A_1'), and 0.44 (A_2''), respectively, consistent with the measured value of Raman-active E' of 0.6 in Ref. [10]. It is interesting to find that all the modes show a positive value of γ, indicative of a normal behavior of softening frequencies with expanding the lattice host [44]. The positive γ indicates a positive coefficient of thermal expansion of monolayer MoS_2 even at low temperatures where only the acoustic modes are excited. This is in contrast to the negative thermal expansion observed

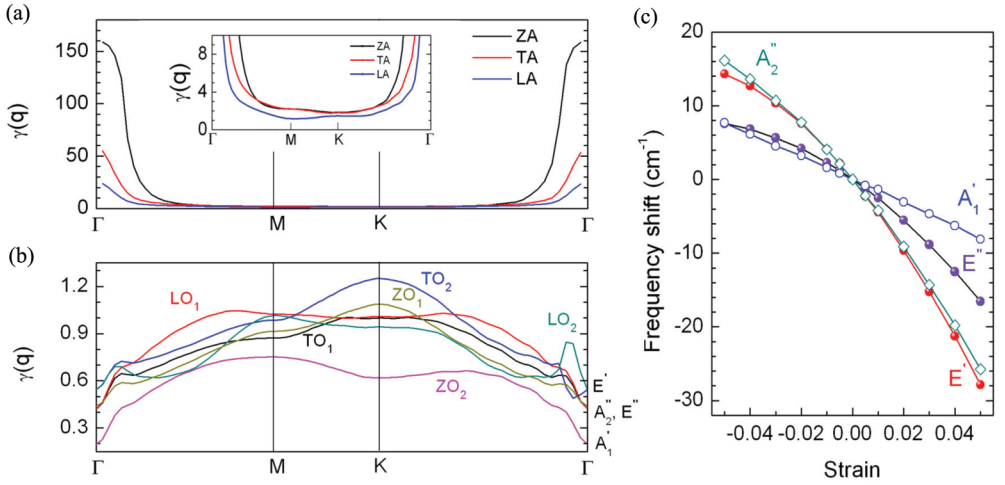

FIG. 3. (Color online) The Grüneissen parameter of acoustic (a) and optical (b) modes of monolayer MoS_2. The inset in (a) is a close-up view. (c) Frequency shift for optical modes under biaxial strain in the sheet.

TABLE I. Phonon parameters of single-layer MoS_2 at Γ for three acoustic modes (labeled according to polarization) and four optical modes (labeled according to symmetry assignment of irreducible representation of the D_{3h} point group): frequency (ω), Grüneissen parameter (γ) determined by biaxial strain, and relaxation time (τ). Note that γ and τ for the three acoustic modes (ZA, TA, and LA) are shown at the cutoff frequency of 0.05 THz.

	ZA	TA	LA	E''	E'	A_1'	A_2''
ω (cm^{-1})	0	0	0	298.2	402.7	423.9	490.5
				289.2[a]	391.7[a]	410.3[a]	476.0[a]
γ	159.71	58.63	25.31	0.42	0.54	0.20	0.44
				0.54[b]	1.06,[c] 0.21,[b] 0.6[d]	0.21[b]	0.53[b]
τ (ps)	6.93	22.17	48.21	16.84	5.50	38.36	5.72
					5.1[e]		2.1[e]

[a]Reference [32].
[b]Reference [46].
[c]γ obtained from Ref. [47] by measuring the shift of the Raman peak through applying uniaxial strain.
[d]γ obtained from Ref. [10] by measuring the shift of the Raman peak through applying uniaxial strain.
[e]Relaxation time (τ) measured for the bulk 2H-MoS_2 phase of the two IR-active modes: E_{1u} and A_{2u} modes corresponding, respectively, to the E' and A_2'' modes of the monolayer case, by analyzing the damping constant of the image dielectric spectrum in Ref. [56].

in graphene at low temperatures due to the negative γ of the ZA mode [45]. The issue of thermal expansion is critical for two-dimensional devices as the different thermal expansion coefficients between samples and substrate can result in strain, which may affect the performance and reliability for electronic device applications. Our results of Grüneissen parameter γ show that monolayer MoS_2 is a credible alternative to graphene in some applications in which a positive thermal expansion monolayer material is preferred. The underlying reason for the difference in thermal-mechanical relationship between MoS_2 and graphene may be due to the suppression of the bending mode in MoS_2 owing to its sandwiched structure. The values of γ for the three acoustic modes at the Γ point are 159.7, 58.6, and 25.3 for ZA, TA, and LA, respectively, which are overwhelmingly larger than those of the optical modes within the whole Brillouin zone. These results show that the anharmonicity is weaker for optical modes than for acoustic modes.

The variation of the frequencies for modes at the Γ point with compressive and tensile strains is plotted in Fig. 3(c), where the frequency shift with strain (δ) is defined as $\Delta\omega(\delta) = \omega(\delta) - \omega(0)$. The different slopes of the δ-$\Delta\omega$ curves reflect the different stiffening or softening behavior of each phonon mode under strain. For the A_1' mode, the slope is the smallest among all the modes, consistent with the smallest γ of the ZO_2 branch within the whole Brillouin zone [Fig. 3(b)]. The eigenvector of this mode shows that the S atoms vibrate in counterphase in direction normal to the plane (Fig. 1) and the Mo plane remains stationary. Thus the frequency is relatively insensitive to the in-plane strain, but quite sensitive to the disturbance normal to the plane such as increasing layers [32], electronic doping, or chemical doping above the planes. In contrast, the E' mode involves the in-plane vibration, and thus is more sensitive to the in-plane strain. Note here that the trends for these two modes are reversed in the case of doping on the layer, where the A_1' mode shows significant softening behavior, whereas the E' mode remains nearly constant [12].

Our study of the larger slope of the E' mode (E_2g for bulk MoS_2) than the A_1' mode (A_1g for bulk MoS_2) with strain is consistent with previous measurements [46,47]. Assuming a linear expansion of the sample with increasing temperature, the frequency shift can also be detected from the evolution of the Raman spectrum for samples at different temperatures. The positive γ is consistent with the redshift of the Raman-active modes with temperature observed in experiments [9,19,48–50].

C. Relaxation time and mean free path based on umklapp process

The phonon relaxation time in real materials can be obtained by the combination of various scattering processes, such as phonon-phonon umklapp scattering, boundary scattering, and defects scattering. By improving sample quality, extrinsic scatters such as defects and grain boundary can be removed. In the present work, we focus on the intrinsic phonon relaxation process in monolayer MoS_2 sheet, thus boundary scattering is not considered. The intrinsic phonon relaxation time associated with phonon-phonon umklapp scattering was derived using an expression given by Klemens based on the time-dependent perturbation theory [51,52], but introducing separate lifetimes (τ_{qs}) for different phonon branches:

$$\frac{1}{\tau_{qs}} = 2\gamma_{qs}^2 \frac{k_B T}{M v^2} \frac{\omega_{qs}^2}{\omega_m}, \tag{4}$$

where M is the atomic mass and ω_m is the Debye frequency, T is the temperature, k_B is the Boltzmann constant, and v is the averaged sound velocity given by the relation $2/v^2 = 1/v_{\mathrm{LA}}^2 + 1/v_{\mathrm{TA}}^2$ around the zone center. It should be noted that a cutoff frequency (ω_c) for the long-wavelength acoustic phonons should be adopted in this formula to avoid the divergence issue [53,54]. In the previous study on bulk graphite, Klemens *et al.* [53] chose the frequency of the ZO′ mode at Γ as the ω_c (around 4 THz) based on the assumption of the onset of cross-plane coupling and heat transport at this frequency. However, for monolayer MoS_2, this assumption cannot be applied as there is no ZO′ mode in the monolayer case. For monolayer graphene flakes and ribbons, a more physical procedure, that is, determining the cutoff frequency by the size of the sample, has been proposed to get rid of the divergence [55–57]. Using this

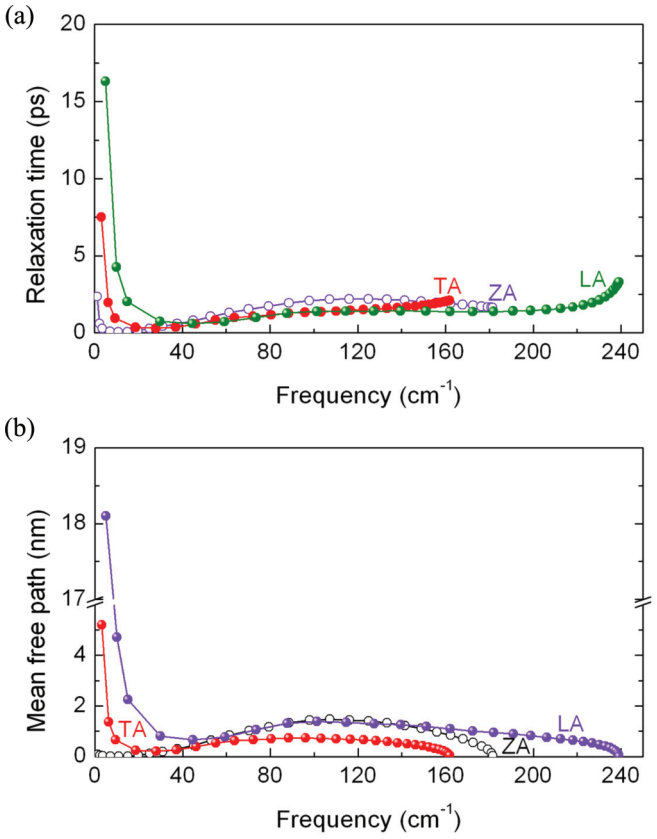

FIG. 4. (Color online) (a) Frequency-dependent relaxation time and (b) mean free path for the three acoustic modes (ZA, TA, and LA) of monolayer MoS_2.

physical model, several theoretical works have been performed to explore various effects on the thermal conductivity of graphene [56,57]. By nondimensionalizing the data based on umklapp scattering rates of phonons and assuming a constant sound velocity within the whole Brillouin zone, Freedman *et al*. recently showed a universal MFP spectrum in crystalline semiconductors and revealed that approximately 90% of the thermal conductivity is contributed from phonons with MFPs in the range between 1 and 200 times that of the MFP of acoustic phonons at the Brillouin zone edge [58], covering the phonon frequencies between 0.5% and 100% of the frequencies of acoustic phonons at the Brillouin zone edge. Based on this scenario, ω_c of 1.2 cm^{-1} is selected here which is 0.5% of the frequency of the LA phonon at the M point ($\sim$240 cm^{-1}).

Figure 4(a) gives the frequency dependence of relaxation time of the LA, TA, and ZA phonons in monolayer MoS_2 sheet. For these acoustic phonon branches, the relaxation time decreases sharply as the frequency of phonons increases. The calculated $\tau(\omega_c)$ for both acoustic and optical branches are compiled in Table I. The values for the ZA, TA, and LA modes are found to be 6.93, 22.17, and 48.21 ps, respectively. The ZA mode shows the shortest relaxation time as an indication of the strongest phonon scattering, being consistent with the largest Grüneissen parameter.

For the four optical modes, the relaxation times are 16.84 ps (E''), 5.50 ps (E'), 38.36 ps (A_1'), and 5.72 ps (A_2''). By fitting the classical dielectric oscillators with the measured IR reflectivity, Sun *et al*. recently obtained the relaxation times for the IR modes E'(5.1 ps) and A_2'' (2.1 ps) [59]. With consideration of the phonon-phonon umklapp scattering, our predicted τ of the in-plane E' mode is in good agreement with the measured value (5.1 ps), whereas for the A_2'' mode the τ is twofold larger than the experimental value. For real materials, the phonon relaxation time can be decomposed into contributions from electron-phonon, phonon-substrate, and phonon-phonon umklapp scattering. For the out-of-plane vibrating A_2'' mode, the contribution from electron-phonon and phonon-substrate coupling is more significant than that in the in-plane E' mode due to the d_{z^2} character in the frontier orbitals [12]. This may account for the calculated larger phonon relaxation time for the A_2'' mode with only considering the umklapp scattering.

For the Raman-active phonons, unfortunately, there is no measured value of the lifetime for comparison. Our result shows that the nonpolar optical E'' (homopolar A_1') mode possesses a much longer τ (three and seven times, respectively) than those of the IR-active E' and A_2'' polar modes. This indicates that the thermal scattering in the optical modes mainly occurs through the polar modes.

A fundamental understanding of the phonon MFP is essential to identify the phonon κ of two-dimensional materials. Based on the mode-dependent τ and group velocity, we obtain the umklapp scattering limited MFP of monolayer MoS_2, which is a key quantity for understanding the size-scaling characteristics of κ. The phonon MFP for the mode at the $\boldsymbol{q}$ point with s polarization is defined as $\lambda_{qs} = V_{qs}\tau_{qs}$. It is well known that the acoustic modes contribute to most of the κ due to their relatively larger velocities than those of the optical modes [23]. Therefore, we only analyze the acoustic modes phonon MFP. The frequency- and mode-dependent phonon MFP dominated by the umklapp process is shown in Fig. 4(b). Similar to relaxation time, for all the phonon branches, MFP decreases obviously with increasing frequency, then increases and decreases slightly. Over the entire frequency regime, the MFP of the LA mode is larger than those of the TA and ZA modes, due to the combined effects from the frequency-dependent relaxation time and group velocities. To define an effective or frequency-independent MFP for each branch, we employed the MFP at truncated frequency (ω_c) as the dominated MFP, beyond which all phonons experience nonballistic transport. The largest dominated MFP among the zone-center acoustic modes is found to be the LA mode with a value of around 18.1 nm, which is much larger than that of the TA mode (5.0 nm). This finding is consistent with the value of 5.2 nm by the recent MD calculation performed by Liu *et al*. [15]. Our calculation shows that the MFP of monolayer MoS_2 sheet is much smaller than that of the graphene ($\sim$775 nm) [20]. Since the sizes of most reported MoS_2 flakes are around 1 μm [60–63], the thermal conduction in these samples is highly likely to be in the diffusive regime according to the predicted dominated MFP. Our study suggests that there appears to be a significant reduction of thermal conduction when the characteristic length, such as the size of the sample or the size of the grain, is reduced down to tens of nanometers as the grain boundary or edge boundary scattering becomes greatly enhanced.

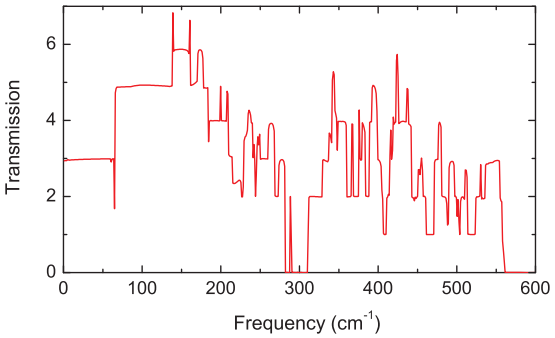

FIG. 5. (Color online) Phonon transmission for monolayer MoS_2 calculated by the NEGF method.

D. Thermal conductivity calculated from NEGF

In this part, we calculate the thermal conductance and thermal conductivity of monolayer MoS_2 by using the NEGF approach. The MoS_2 sheet is modeled by creating an orthogonal supercell containing 144 atoms with assigning the armchair direction as the thermal conducting direction. Periodic boundary condition is applied in both the heat current direction and in-plane transverse direction. As it is computationally highly demanding by DFPT calculation for this system, here we use the Vienna *ab initio* simulation package (VASP) package [64] with the Perdew-Burke-Ernzerhof functional to obtain the Hessian matrix by shifting individual atoms in the supercell and determine the forces induced on all other atoms. Figure 5 shows the obtained phonon-transmission spectrum. The difference in mode frequency between Figs. 1 and 5 due to the different approaches is small. The calculated thermal conductance is 1.06 nW/K for the sample with a width of 1.27 nm. Assuming a thickness of the MoS_2 sheet of 0.65 nm, the scaled thermal conductance, defined as thermal conductance per unit area σ/S, amounts to 1.28 nW K^{-1} nm^{-2}.

The thermal conductivity κ of a finite sample is related to the thermal conductance σ by $\kappa = \sigma l/S$, where l is the length of the sample, and S is its cross section. Within the ballistic regime ($l < \lambda$, λ is phonon MFP), the κ is linearly correlated with the length since the conductance σ is length independent [21]. In contrast, when the sample length is beyond mean free path ($l > \lambda$), the transport is diffusive and κ is less sensitive to the variation of the length. It was proposed [21] that from the NEGF calculated ballistic thermal conductance, one may estimate the size-independent thermal conductivity of a sample with the relation $\kappa = \sigma\lambda/S$, where λ is the phonon mean free path. Using this approach, the room temperature thermal conductivity of single-layer graphene calculated from NEGF is 3410 W m^{-1} K^{-1} [21], which is comparable with the experimental measurements [65]. Since thermal conductivity in semiconductors results mainly from phonons with long MFP [58,66], to derive the κ of MoS_2, here we use the dominated MFP of the zone-center LA mode ($\lambda = 18.1$nm) obtained in the lattice vibrational modes section. The room temperature (300 K) thermal conductivity of monolayer MoS_2 is found to be 23.2 W m^{-1} K^{-1}. It is worth mentioning that if the phonon MFP of 5.2 nm (by the MD calculation in Ref. [15]) is adopted, the κ is about 6.66 W m^{-1} K^{-1}, which is in the same order of magnitude with the MD results of 1.35 W m^{-1} K^{-1} [15].

Our predicted κ of 23.2 W m^{-1} K^{-1} of MoS_2 is much smaller than the ultrahigh thermal conductivity (4800–5600 W m^{-1} K^{-1}) of graphene [65]. Very recently, the thermal conductivity of monolayer MoS_2 was obtained from temperature-dependent Raman spectroscopy measurement [67]. The measured value was found to be about 34.5 $\pm$ 4 W m^{-1} K^{-1}, which is in good agreement with our calculation result. Since the scaled thermal conductance σ/S value of 1.28 nW K^{-1} nm^{-2} for MoS_2 is only slightly smaller than that of graphene ($\sim$4.1 nW K^{-1} nm^{-2} from Ref. [68]) with the same width, the 100-fold reduction of κ in MoS_2 arises from the much shorter MFP in MoS_2 compared with graphene.

Experimentally measured values of κ of MoS_2 are from 0.4–1.59 W m^{-1} K^{-1} [17,18], 34.5 $\pm$ 4 W m^{-1} K^{-1} [67], to around 52 W m^{-1} K^{-1} [19]. The large discrepancy in experimental measurements may originate from different sample quality, measurement methods, and accuracy. For many two-dimensional nanomaterials, it was found that various factors, such as the size of sample, substrate, defects, and strain, etc. can have remarkable effects on their thermal conductivity [56,57]. It is thus expected that similar effects may also exist in the thermal transport of MoS_2 monolayer. Undoubtedly, the determination of the intrinsic thermal conductivity of MoS_2 monolayer in the absence of phonon scattering from point defects, grain boundaries, and edges is an important step towards fully understanding its thermal properties. Thus numerical simulations will definitely facilitate the understanding of heat conduction in monolayer MoS_2 sheet. MD has the obvious advantage that it does not rely on any thermodynamic-limit assumption, and is thus applicable to model nanoscale systems with real geometries. However, the calculated κ may rely on the interatomic empirical potentials used. The combination of first-principles calculation and the NEGF method has been commonly used to describe the ballistic phonon transport. In the present work, by adopting the umklapp phonon-phonon scattering limited MFP, our calculation provides an estimation of the intrinsic thermal conductivity. However, the intrinsic relaxation time of phonon-phonon umklapp scattering is calculated from an empirical equation based on the time-dependent perturbation theory [51,52]. Thus phonon scattering rates obtained fully from *ab initio* density functional theory calculations [69] without any adjustable parameters is still indispensable to determine the dominated phonon MFP.

IV. CONCLUSION

An in-depth understanding of the lattice vibrational modes and intrinsic thermal conductivity of MoS_2 is highly important to speed up its potential applications in nanoelectronics and thermoelectric energy devices. Based on the DFPT calculations, we have obtained the Grüneissen parameters and the umklapp scattering limited relaxation time of phonons in monolayer MoS_2. The calculated phonon lifetime of the IR-active modes is in good agreement with experimental results. The dominated phonon mean free path of the monolayer MoS_2 sheet is around 18.1 nm, about 30-fold smaller than that of graphene. By using the NEGF approach combined with the

obtained mean free path, the intrinsic thermal conductivity of monolayer MoS_2 at room temperature is found to be around 23.2 $W\,m^{-1}\,K^{-1}$, around two orders smaller than that of grapheme, due to the significantly shorter phonon mean free path than that of graphene.

ACKNOWLEDGMENTS

The authors gratefully acknowledge the financial support from the Agency for Science, Technology and Research (A*STAR), Singapore and the use of computing resources at the A*STAR Computational Resource Centre, Singapore.

[1] Q. H. Wang, K. Kalantar-Zadeh, A. Kis, J. N. Coleman, and M. S. Strano, Nat. Nanotechnol. **7**, 699 (2012).
[2] M. Chhowalla, H. S. Shin, G. Eda, L.-J. Li, K. P. Loh, and H. Zhang, Nat. Chem. **5**, 263 (2013).
[3] S. Sim, J. Park, J.-G. Song, C. In, Y.-S. Lee, H. Kim, and H. Choi, Phys. Rev. B **88**, 075434 (2013).
[4] H. Shi, R. Yan, S. Bertolazzi, J. Brivio, B. Gao, A. Kis, D. Jena, H. G. Xing, and L. Huang, ACS Nano **7**, 1072 (2013).
[5] K. Kaasbjerg, K. S. Thygesen, and K. W. Jacobsen, Phys. Rev. B **85**, 115317 (2012).
[6] K. Kaasbjerg, K. S. Thygesen, and A.-P. Jauho, Phys. Rev. B **87**, 235312 (2013).
[7] K. Dolui, C. D. Pemmaraju, and S. Sanvito, ACS Nano **6**, 4823 (2012).
[8] P. Johari and V. B. Shenoy, ACS Nano **6**, 5449 (2012).
[9] T. Livneh and E. Sterer, Phys. Rev. B **81**, 195209 (2010).
[10] Y. Wang, C. Cong, C. Qiu, and T. Yu, Small **9**, 2857 (2013).
[11] C. Lee, H. Yan, L. E. Brus, T. F. Heinz, J. Hone, and S. Ryu, ACS Nano **4**, 2695 (2010).
[12] B. Chakraborty, A. Bera, D. V. S. Muthu, S. Bhowmick, U. V. Waghmare, and A. K. Sood, Phys. Rev. B **85**, 161403(R) (2012).
[13] Y. Ge and A. Y. Liu, Phys. Rev. B **87**, 241408(R) (2013).
[14] M. Buscema, M. Barkelid, V. Zwiller, H. S. J. van der Zant, G. A. Steele, and A. Castellanos-Gomez, Nano Lett. **13**, 358 (2013).
[15] X. Liu, G. Zhang, Q.-X. Pei, and Y.-W. Zhang, Appl. Phys. Lett. **103**, 133113 (2013).
[16] J.-W. Jiang, H. S. Park, and T. Rabczuk, J. Appl. Phys. **114**, 064307 (2013).
[17] R. C. McLaren, M.S. dissertation, University of Illinois, 2009.
[18] J.-Y. Kim, S. M. Choi, W.-S. Seo, and W.-S. Cho, Bull. Korean Chem. Soc. **31**, 3225 (2010).
[19] S. Sahoo, A. P. S. Gaur, M. Ahmadi, M. J.-F. Guinel, and R. S. Katiyar, J. Phys. Chem. C **117**, 9042 (2013).
[20] S. Ghosh, I. Calizo, D. Teweldebrhan, E. P. Pokatilov, D. L. Nika, A. A. Balandin, W. Bao, F. Miao, and C. N. Lau, Appl. Phys. Lett. **92**, 151911 (2008).
[21] J. Lan, J.-S. Wang, C. K. Gan, and S. K. Chin, Phys. Rev. B **79**, 115401 (2009).
[22] D. L. Nika, E. P. Pokatilov, A. S. Askerov, and A. A. Balandin, Phys. Rev. B **79**, 155413 (2009).
[23] Z.-Y. Ong and E. Pop, Phys. Rev. B **84**, 075471 (2011).
[24] P. Giannozzi *et al.*, J. Phys.: Condens. Matter **21**, 395502 (2009).
[25] T. Böker, R. Severin, A. Müller, C. Janowitz, R. Manzke, D. Voss, P. Krüger, A. Mazur, and J. Pollmann, Phys. Rev. B **64**, 235305 (2001).
[26] J.-S. Wang, J. Wang, and N. Zeng, Phys. Rev. B **74**, 033408 (2006).
[27] J.-S. Wang, N. Zeng, J. Wang, and C. K. Gan, Phys. Rev. E **75**, 061128 (2007).
[28] T. J. Wieting and J. L. Verble, Phys. Rev. B **3**, 4286 (1971).
[29] P. Tonndorf, R. Schmidt, P. Böttger, X. Zhang, J. Börner, A. Liebig, M. Albrecht, C. Kloc, O. Gordan, D. R. T. Zahn, S. Michaelis de Vasconcellos, and R. Bratschitsch, Opt. Express **21**, 4908 (2013).
[30] L. Sun, J. Yan, D. Zhan, L. Liu, H. Hu, H. Li, B. K. Tay, J.-L. Kuo, C.-C. Huang, D. W. Hewak, P. S. Lee, and Z. X. Shen, Phys. Rev. Lett. **111**, 126801 (2013).
[31] Y. Cheng, Z. Zhu, and U. Schwingenschlögl, RSC Adv. **2**, 7798 (2012).
[32] A. Molina-Sánchez and L. Wirtz, Phys. Rev. B **84**, 155413 (2011).
[33] C. Ataca, M. Topsakal, E. Aktürk, and S. Ciraci, J. Phys. Chem. C **115**, 16354 (2011).
[34] G. Plechinger, S. Heydrich, J. Eroms, D. Weiss, C. Schüller, and T. Korn, Appl. Phys. Lett. **101**, 101906 (2012).
[35] H. Zeng, B. Zhu, K. Liu, J. Fan, X. Cui, and Q. M. Zhang, Phys. Rev. B **86**, 241301(R) (2012).
[36] X. Zhang, W. P. Han, J. B. Wu, S. Milana, Y. Lu, Q. Q. Li, A. C. Ferrari, and P. H. Tan, Phys. Rev. B **87**, 115413 (2013).
[37] M. Boukhicha, M. Calandra, M.-A. Measson, O. Lancry, and A. Shukla, Phys. Rev. B **87**, 195316 (2013).
[38] P. H. Tan, W. P. Han, W. J. Zhao, Z. H. Wu, K. Chang, H. Wang, Y. F. Wang, N. Bonini, N. Marzari, N. Pugno, G. Savini, A. Lombardo, and A. C. Ferrari, Nat. Mater. **11**, 294 (2012).
[39] C. H. Lui and T. F. Heinz, Phys. Rev. B **87**, 121404(R) (2013).
[40] Y. Cai, L. Zhang, Q. Zeng, L. Cheng, and Y. Xu, Solid State Commun. **141**, 262 (2007).
[41] Y. Cai, L. Zhang, Q. Zeng, L. Cheng, and Y. Xu, Phys. Rev. B **74**, 174301 (2006).
[42] J. Zou and A. Balandin, J. Appl. Phys. **89**, 2932 (2001).
[43] N. Mounet and N. Marzari, Phys. Rev. B **71**, 205214 (2005).
[44] Y. Cai, C. Zhang, and Y. P. Feng, Phys. Rev. B **84**, 094107 (2011).
[45] B. D. Kong, S. Paul, M. B. Nardelli, and K. W. Kim, Phys. Rev. B **80**, 033406 (2009).
[46] C. Rice, R. J. Young, R. Zan, U. Bangert, D. Wolverson, T. Georgiou, R. Jalil, and K. S. Novoselov, Phys. Rev. B **87**, 081307(R) (2013).
[47] Hiram J. Conley, Bin Wang, Jed I. Ziegler, Richard F. Haglund, Jr., Sokrates T. Pantelides, and Kirill I. Bolotin, Nano Lett. **13**, 3626 (2013).
[48] S. Najmaei, Z. Liu, P. M. Ajayan, and J. Lou, Appl. Phys. Lett. **100**, 013106 (2012).
[49] N. A. Lanzillo, A. Glen Birdwell, M. Amani, F. J. Crowne, P. B. Shah, S. Najmaei, Z. Liu, P. M. Ajayan, J. Lou, M. Dubey,

S. K. Nayak, and T. P. O'Regan, Appl. Phys. Lett. **103**, 093102 (2013).
[50] J. A. Wilson and A. D. Yoffe, Adv. Phys. **18**, 193 (1969).
[51] P. G. Klemens, J. Wide Bandgap Mater. **7**, 332 (2000).
[52] P. G. Klemens, Int. J. Thermophys. **22**, 265 (2001).
[53] P. G. Klemens and D. F. Pedraza, Carbon **32**, 735 (1994).
[54] D. L. Nika, S. Ghosh, E. P. Pokatilov, and A. A. Balandin, Appl. Phys. Lett. **94**, 203103 (2009).
[55] D. L. Nika, E. P. Pokatilov, and A. A. Balandin, Phys. Status Solidi B **248**, 2609 (2011).
[56] D. L. Nika and A. A. Balandin, J. Phys.: Condens. Matter **24**, 233203 (2012).
[57] A. A. Balandin, Nat. Mater. **10**, 569 (2011).
[58] J. P. Freedman, J. H. Leach, E. A. Preble, Z. Sitar, R. F. Davis, and J. A. Malen, Sci. Rep. **3**, 2963 (2013).
[59] Q.-C. Sun, D. Mazumdar, L. Yadgarov, R. Rosentsveig, R. Tenne, and J. L. Musfeldt, Nano Lett. **13**, 2803 (2013).
[60] B. Chakraborty, H. S. S. Ramakrishna Matte, A. K. Sood, and C. N. R. Rao, J. Raman Spectrosc. **44**, 92 (2013).
[61] H. Li, Q. Zhang, C. Chong Ray Yap, B. Kang Tay, T. Hang Tong Edwin, A. Olivier, and D. Baillargeat, Adv. Funct. Mater. **22**, 1385 (2012).
[62] S.-L. Li, H. Miyazaki, H. Song, H. Kuramochi, S. Nakaharai, and K. Tsukagoshi, ACS Nano **6**, 7381 (2012).
[63] S. Tongay, J. Zhou, C. Ataca, K. Lo, T. S. Matthews, J. Li, J. C. Grossman, and J. Wu, Nano Lett. **12**, 5576 (2012).
[64] G. Kresse and J. Furthmüller, Phys. Rev. B **54**, 11169 (1996).
[65] A. A. Balandin, S. Ghosh, W. Bao, I. Calizo, D. Teweldebrhan, F. Miao, and C. N. Lau, Nano Lett. **8**, 902 (2008).
[66] J. A. Johnson, A. A. Maznev, J. Cuffe, J. K. Eliason, A. J. Minnich, T. Kehoe, Clivia M. Sotomayor Torres, G. Chen, and K. A. Nelson, Phys. Rev. Lett. **110**, 025901 (2013).
[67] R. Yan, J. R. Simpson, S. Bertolazzi, J. Brivio, M. Watson, X. Wu, A. Kis, T. Luo, A. R. H. Walker, and H. G. Xing, ACS Nano **8**, 986 (2014).
[68] Y. Xu, X. Chen, B.-L. Gu, and W. Duan, Appl. Phys. Lett. **95**, 233116 (2009).
[69] W. Li, J. Carrete, and N. Mingo, Appl. Phys. Lett. **103**, 253103 (2013).